



Magnetic Field Gradient Across the Flank Magnetopause

Zdeněk Němeček^{1*}, Kostiantyn Grygorov¹, Jana Šafránková¹, Jiří Šimůnek² and Gilbert Pi¹

¹Charles University, Faculty of Mathematics and Physics, Prague, Czechia, ²Institute of Atmospheric Physics, Czech Academy of Sciences, Prague, Czechia

Magnetic pressure inside the magnetopause is usually balanced with a sum of thermal plasma and magnetic pressures on the magnetosheath side. However, observations reveal that the magnetosheath magnetic field can be frequently larger than that in the magnetosphere (inverse magnetic field gradient across the magnetopause), and thus, the enhanced pressure from the magnetosheath side seems to be uncompensated. Such events are rare in the subsolar region, but their occurrence rate increases toward flanks. The analysis, based on statistical processing of about 35,000 THEMIS magnetopause crossings collected in the course of the years 2007–2017, shows that these events are more frequently observed under enhanced geomagnetic activity that is connected with a strong southward IMF. Case studies reveal that such a state of the magnetopause boundary layers can persist for several hours. This study discusses conditions and mechanisms keeping the pressure balance across the magnetopause under these conditions.

Keywords: magnetosphere, magnetopause, magnetosheath, pressure balance, magnetic field gradient, inverse gradient, geomagnetic indices

OPEN ACCESS

Edited by:

Hiroshi Hasegawa,
Japan Aerospace Exploration Agency,
Japan

Reviewed by:

Anton Artemyev,
Space Research Institute (RAS),
Russia
Emilia Kilpua,
University of Helsinki, Finland

*Correspondence:

Zdeněk Němeček
zdenek.nemecek@mff.cuni.cz

Specialty section:

This article was submitted to
Space Physics,
a section of the journal
Frontiers in Astronomy and Space
Sciences

Received: 16 September 2021

Accepted: 13 October 2021

Published: 17 November 2021

Citation:

Němeček Z, Grygorov K, Šafránková J,
Šimůnek J and Pi G (2021) Magnetic
Field Gradient Across the
Flank Magnetopause.
Front. Astron. Space Sci. 8:778234.
doi: 10.3389/fspas.2021.778234

1 INTRODUCTION

The magnetopause is a current sheet forming the boundary between the magnetic pressure of the Earth's dipole on the one side and the shocked supersonic solar wind with an embedded interplanetary magnetic field (IMF) on the other side. However, the total pressure even at the subsolar magnetopause is not exactly equal to the solar wind dynamic pressure (e.g., Spreiter et al., 1966; Samsonov et al., 2012), and the total magnetospheric magnetic field is a superposition of the magnetic field of the Earth's dipole field and the field of several magnetospheric current systems (e.g., Tsyganenko and Andreeva, 2015). Since the magnetopause position is given by the total pressure balance of plasmas and fields on either side, the magnetopause is constantly moving back and forth due to solar wind pressure variations at all timescales. The motion is controlled by a combination of direct solar wind variations (predominantly by changes in the solar wind dynamic pressure) and surface waves such as Kelvin-Helmholtz (Haaland et al., 2019). At the flanks, the latter probably plays a larger role because some theories (e.g., Kavosi and Raeder, 2015; Fadanelli et al., 2018) suppose that waves are excited by local instabilities at the dayside and propagate toward the flanks. At present, there does not seem to be a clear consensus about whether surface waves are more frequent on the dawn or dusk flanks; nevertheless, a dawn-dusk asymmetry of the macroscopic parameters was a subject of the study by Haaland et al. (2020), and they found, based on MMS data, that the dawn magnetopause is thicker than at dusk, while the dusk flank is more dynamic, with a higher average normal velocity.

The magnetopause is one of the most complex boundaries in space because its formation involves electrical currents, gradients of the plasma density and pressure, flow shear, and/or anisotropy of velocity distributions of particles (Němeček et al., 2020). Therefore, different forms of free energy are accessible at and around the magnetopause, and a variety of instabilities such as current-driven (e.g., magnetic reconnection (Paschmann et al., 1979; Sonnerup et al., 1981)), flow shear-driven (e.g., nonlinear Kelvin-Helmholtz waves (Hasegawa et al., 2004, 2009)), and/or anisotropy-driven (e.g., mirror) instabilities can be excited there (Hasegawa, 2012), but also diffusion (e.g., Treumann et al., 1995) and impulsive penetration (e.g., Lemaire et al., 1979) have been suggested to enable transport across the magnetopause. In addition, the magnetopause is curved on a large scale, and thus, when the upstream flow is super-magnetosonic, it is exposed to a highly time-varying and inhomogeneous plasma of the magnetosheath, the region of a shocked solar wind situated between the magnetopause and bow shock (Berchem and Russell, 1982). Moreover, when the magnetopause thickness is comparable to (or less than) the ion Larmor radius, the boundary structure could also be affected by kinetic effects (Cai et al., 1990; Nakamura et al., 2010).

Due to the focus on processes responsible for the transfer of momentum and energy across the magnetopause and the associated impact on magnetospheric dynamics, much attention has been paid to the dayside magnetopause near the SunEarth line. The interaction between the IMF and geomagnetic field at the dayside magnetopause has a direct consequence on the large-scale plasma circulation in the magnetosphere and magnetically connected ionosphere. The magnetopause flanks and possible dawn-dusk asymmetries have received less attention, partly because interactions along the flanks probably have a smaller effect on the geomagnetic activity and partly due to results of observations in this region which demonstrate a small difference of boundary layer characteristics between dayside and flanks. A study of Artemyev et al. (2017) showed that plasma and magnetic field characteristics are very similar for boundary layers observed at the lunar orbit ($\approx 55 R_E$) and farther downtail as far as $\approx 200 R_E$ and that the dynamical magnetosheath pressure does not contribute to the pressure balance across the boundary layer at these distances. Furthermore, Lukin et al. (2020) compared the characteristics of magnetic field and plasma populations during simultaneous magnetopause crossings, which are separated by about $50 R_E$ (dayside vs night sides), and found that the magnetosheath current sheet profiles are similar at these two locations. Nevertheless, a flank magnetopause configuration and dynamics are critical for understanding the transport of magnetosheath plasma toward the magnetotail (Wing et al., 2014; Haaland et al., 2019).

Němeček et al. (2002), Zastenker et al. (2002), and Šafránková et al. (2002) compared the magnetosheath measurements with calculations using the Spreiter gasdynamic models of the magnetosheath plasma flow (Spreiter et al., 1966) and IMF modification (Spreiter and Stahara, 1980). They have shown that an average behavior of magnetosheath parameters is predicted rather well by these models. However, they noted

that large variations of the ion flux and magnetic field magnitude in the magnetosheath are not always predicted by these models because their variations originated in the magnetosheath itself (or in the foreshock). Such structures are moving tailward along the magnetopause together with the plasma flow (Shevyrev et al., 2003). A suggested explanation for these structures (using the similarity of plasma and magnetic field variation levels) is that they are created near the bow shock as compressional waves.

On the sunward side, the Earth's magnetic field has mainly compressed dipolar structure, whereas the field is stretched out and forms the magnetotail that consists of the northern and southern lobes separated by the plasma sheet on the night side. Due to lower densities and temperatures in lobes than in the plasma sheet, a force imposed on the magnetotail toward its center is balanced by the plasma pressure in the plasma sheet (Coroniti and Kennel, 1972). While the pressure equilibrium exists most of the time, the plasma sheet can also be highly dynamic because the lobes and plasma sheet store energy, which is often released in explosive events during substorms and storms (McPherron et al., 2011).

Both the solar wind and ionosphere can be sources of the plasma sheet plasma. Wing et al. (2014) and later Kistler (2020) have summarized knowledge on the solar wind entry and transport to the plasma sheet for different IMF orientations. Generally, during a northward IMF, the plasma sheet ion spectrum is well-described by two populations. The colder component ($< \approx 1$ keV) is identified as being the solar wind origin because it is only slightly hotter than in the adjacent magnetosheath plasma. This cold and dense plasma sheet occurs after several hours of northward IMF and is observed predominantly along the flanks and at high magnetic latitudes (e.g., Fujimoto et al., 1998) as a result of double cusp or lobe reconnection at the dayside (e.g., Song and Russell, 1992; Sandholt et al., 1999; Lavraud et al., 2006) or enters from the flanks through Kelvin-Helmholtz instability (Sorathia et al., 2019). According to Yu et al. (2020), the cold and dense plasma sheet probably contributes to the production of storm-time energetic particles (Borovsky et al., 1997) and can result in stronger ring currents during the main phase of storms (e.g., Lavraud et al., 2006) and can also lead to the mass loading of the magnetotail. Therefore, it may have effects on substorms (e.g., Fu et al., 2012) and reduction of the reconnection rate (e.g., Toledo-Redondo et al., 2016).

On the other hand, the source of the hotter component ($> \approx 3$ keV) could either be from the ionosphere or from the solar wind plasma that enters farther down the tail and is heated during its transport; however, the cusp entry leads also to a hotter population. The ionospheric plasma has access to the plasma sheet through ion outflow over a wide range of energies that occur throughout the auroral oval and in the polar cap (Li et al., 2013). In the polar cap, the ion escape is mainly due to the ambipolar electric field, and in the auroral regions, local wave acceleration energizes ionospheric plasma to higher energies. During storms, O^+ from both the nightside auroral region and dayside cusp regions enters the plasma sheet (Kistler et al., 2019). Statistical studies have shown that the O^+ content in the plasma sheet

increases with both geomagnetic activity (K_p) and solar EUV (F10.7) (Mouikis et al., 2010), and investigations of the storm-time ring current (e.g., Mouikis et al., 2019) have identified a significant fraction of the energy density that is carried by O^+ , indicating the importance of the ionospheric source. Němeček et al. (2016) studied the influence of these effects on the magnetopause location and showed that increased ionospheric conductivity leads to its inward motion.

During southward IMF conditions, reconnection occurs at the magnetopause on the dayside at low latitudes. The cold and dense plasma can also be observed along both flanks, but the density is smaller than during northward IMF. Thomsen et al. (2003) and Lavraud and Jordanova (2007) investigated the transition when a period of northward IMF is followed by a strongly southward IMF, driving a storm. They have suggested that this dense plasma can load the near-Earth plasma sheet and then get driven into the inner magnetosphere when the IMF turns southward, creating a strong ring current. This would imply that at least at the beginning of a storm, the ring current is formed by solar wind plasma (Kistler, 2020).

Magnetic pressure inside the magnetopause is usually balanced with a sum of thermal plasma pressure and magnetic pressure on the magnetosheath side, but at about 9% of magnetopause crossings, the THEMIS spacecraft encounter the situation when the magnetosheath magnetic field is larger than that in the magnetosphere, and therefore, the enhanced pressure from the magnetosheath side seems to be uncompensated. We call this effect an inverse magnetic gradient across the magnetopause. We investigate the magnetic gradient across the magnetopause and discuss conditions favorable for the creation of an inverse magnetic gradient. An extensive statistical study reveals a large southward IMF in connection with enhanced geomagnetic activity as necessary conditions.

2 DATA PROCESSING

The analysis is based on observations of all THEMIS probes (Angelopoulos, 2008) and covers a half of the solar cycle (2007–2017). The available plasma (McFadden et al., 2008a) and magnetic field (Auster et al., 2008) data were surveyed by an automated routine based on a determination of scanned regions (solar wind, magnetosheath, and magnetosphere). The identification of regions is based on ion and electron densities and temperatures and magnetic field strength. We are using spin resolution ground moments whenever available, otherwise we apply the onboard moments. The solar wind parameters from the OMNI database were lagged on the expected propagation time from the bow shock nose. The identification method is analogous to that suggested by Jelínek et al. (2012), but it is applied on the search for individual magnetopause crossings.

The routine provided about 36,000 magnetopause crossing candidates. We have calculated the location predicted by the Lin et al. (2010) model for them, and all candidates exhibiting difference between predicted and observed distances from the Earth larger than $1.5 R_E$ were checked by a visual inspection of corresponding plots of the plasma and magnetic field, and events

under doubt were discarded. The set includes single crossings as well as a series of multiple crossings that were usually observed close to the apogee of a particular spacecraft. The visual inspection left 34,699 crossings for a further processing.

The time and location of each crossing were complemented with the upstream magnetic field and plasma parameters. We are using wind data lagged on the expected propagation time as a proxy of upstream conditions. Five-minute averages of the spin resolution magnetic field strength, B_{MSH} , the ion density, N_{MSH} , velocity, V_{MSH} , and ion temperature, T_{MSH} , measured by THEMIS just outbound the magnetopause in the magnetosheath and the magnetic field strength just inbound the magnetopause, B_{MSP} , were added for the later processing. In order to account for the uncertainty of the identification of the exact time of magnetopause crossings by our automated routine, we have skipped 1 min on both sides of a particular crossing.

3 MAGNETIC GRADIENT ACROSS THE MAGNETOPAUSE

A distribution of THEMIS crossings projected onto the XY GSM plane is shown in the top left panel of **Figure 1**. Note that we limited our study to $X_{GSE} > -5 R_E$ because the number of crossings behind this limit is very low. We also did not analyze crossings observed by THEMIS B and C at the lunar orbit because the magnetopause is formed in a different way at these distances. Whereas the ram pressure of the solar wind is principal for the formation of the dayside magnetopause, the solar wind flow is nearly parallel with the magnetopause at far flank locations. We have further divided the crossings into three subsets according to the angle, α , between the radius vector and X-axis: subsolar ($|\alpha| < 30^\circ$), near flank ($30^\circ < |\alpha| < 60^\circ$), and distant flank ($|\alpha| > 60^\circ$) that are distinguished by colors in **Figure 1**. We further selected events satisfying a condition $B_{MSH}/B_{MSP} > 1$ that are a dominant subject of the present study. They are indicated by blue crosses, and their number is sufficient to exclude a possibility that they can be attributed to measuring errors. We can note that a relative number of these crossings increases toward the flanks with no apparent dawn-dusk asymmetry. For this reason, we combine data from dawn and dusk sectors in further analysis.

A portion of events exhibiting an inverse magnetic gradient is illustrated in the bottom panel of **Figure 1**, where the B_{MSH}/B_{MSP} ratio is plotted as a function of α . The gray crosses stand for individual crossings, and the red bars show medians in the angle bins. We can see that this median is about constant and equal to ≈ 0.65 in the subsolar region and then starts to increase toward unity at flanks, but it does not reach the blue dashed line standing for $B_{MSH}/B_{MSP} = 1$. These observations are quantified in **Table 1**. The first row in the table presents the number of events in $|\alpha|$ subsets that decrease toward the flank because an apogee of the THEMIS A, D, and E spacecraft is insufficient to cross the flank magnetopause when the solar wind pressure is low. On the other hand, the number of crossings satisfying a condition of $B_{MSH} >$

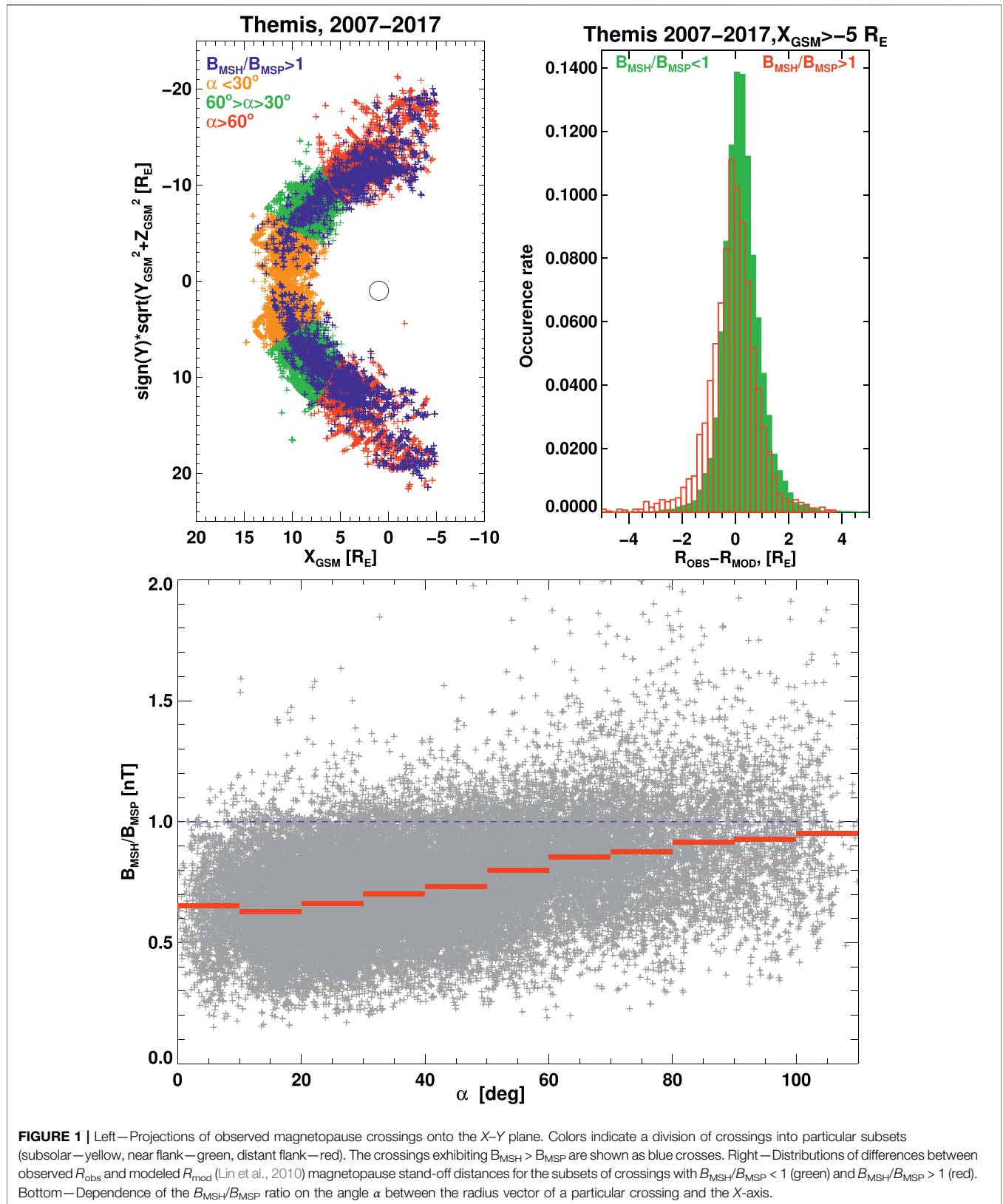


TABLE 1 | Longitudinal distribution of the magnetopause crossings projected onto the equatorial plane.

	All events	$\alpha < 30^\circ$	$30^\circ < \alpha < 60^\circ$	$\alpha > 60^\circ$
All events	34, 699	13, 215	13, 933	7, 551
$B_{\text{MSH}} < B_{\text{MSP}}$	28, 988	12, 092	11, 845	5, 051
$B_{\text{MSH}} > B_{\text{MSP}}$	3, 041	216	979	1, 846

B_{MSP} increases with increasing α and reaches 25% of all crossings in the far flank region.

The top right-hand panel in **Figure 1** shows the distribution of differences between observed and modeled magnetopause stand-off distances. We have checked several empirical magnetopause models, but we decide to use the Lin et al. (2010) model because it explicitly contains the effect of the IMF strength on the magnetopause location. The histograms are plotted for $B_{\text{MSH}} < B_{\text{MSP}}$ (green) and $B_{\text{MSH}} > B_{\text{MSP}}$ (red) events separately. One can note that $B_{\text{MSH}} > B_{\text{MSP}}$ events are generally located closer to the Earth than the “standard” events with a larger magnetic field on the magnetospheric side. We also plotted similar histograms for our subsets and fitted them with Gaussian distributions. The parameters of distributions (full width at half maximum (FWHM) and center) are surveyed in **Table 2**.

Table 2 shows that the Lin et al. (2010) model describes the position of the magnetopause rather well, and the deviations of model locations from observations are lower than $0.2 R_E$ with an exception of the near-flank region. The shift of crossings with $B_{\text{MSH}}/B_{\text{MSP}} > 1$ toward the Earth by about $0.2 R_E$ can be observed in all regions. Since B_{MSH} is actually IMF compressed at the bow shock and the IMF strength is included in the model, it indicates that the effect of the IMF strength on the magnetopause location is not limited by the pressure but influences the whole interaction process. On the other hand, we can see only a slight enlargement of the prediction uncertainty described by FWHM for the crossings with $B_{\text{MSH}}/B_{\text{MSP}} > 1$, but we are operating with a small number of events (**Table 1**) for an ultimate conclusion.

3.1 Upstream Conditions

The previous section has shown that the observations of an inverse magnetic gradient across the magnetopause are rather frequent; the probability of its observations increases with the distance from the subsolar point and reaches nearly 25% at the terminator. In search for the conditions favorable for its formation, we started with an analysis of upstream conditions. We have plotted distributions of the ion density, velocity, and dynamic pressure separately for events with $B_{\text{MSH}} > B_{\text{MSP}}$ and $B_{\text{MSH}} < B_{\text{MSP}}$, but we did not find any systematic difference

among them, thus we are not showing these plots. The only clear dependence of $B_{\text{MSH}}/B_{\text{MSP}}$ on upstream conditions was found for the IMF strength and IMF cone angle (the angle between the IMF and solar wind velocity vectors) as **Figure 2** demonstrates.

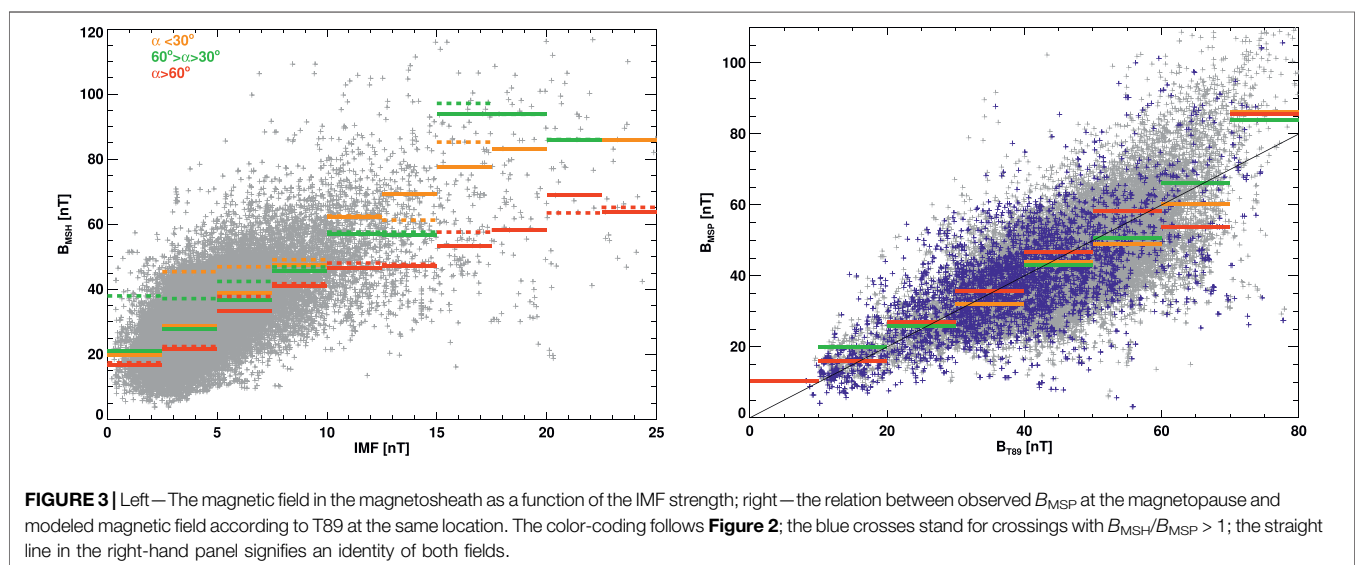
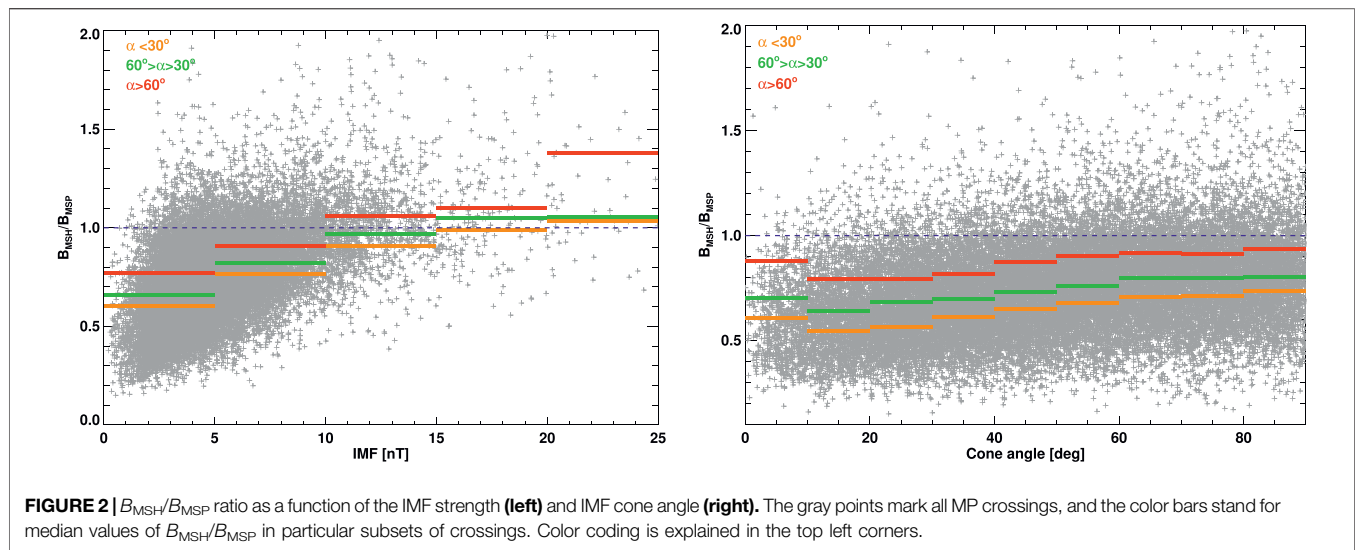
The gray points stand for values corresponding to individual crossings, and color bars show medians in IMF or cone angle bins for the subsolar (yellow), near flank (green), and distant (red) flank. Consistently with the bottom panel in **Figure 1**, the median $B_{\text{MSH}}/B_{\text{MSP}}$ ratio increases with the distance from the subsolar point, but the left panel shows that it also increases with an increasing IMF strength (left panel) in a monotonic way, and it exceeds unity even in the subsolar region if the IMF strength is sufficiently high. We should note that we made plots like those in **Figure 2** for the IMF B_Y and B_Z components, and the results were similar to the $B_{\text{MSH}}/B_{\text{MSP}}$ dependence on the IMF strength.

The clear increase of $B_{\text{MSH}}/B_{\text{MSP}}$ with the cone angle (right panel) starts at about 30° in all magnetopause segments. It is hard to say whether a little larger median ratio observed for a nearly radial field is the real physical effect or a product of limited statistics in this cone angle bin. Nevertheless, it is observed in all three magnetopause regions. The number of points above the blue dashed line (events exhibiting the inverse gradient) increases with the cone angle, but the medians are below unity in all magnetopause segments.

A larger value of the $B_{\text{MSH}}/B_{\text{MSP}}$ can be caused either by too large B_{MSH} or too low B_{MSP} . Let us first check B_{MSH} that is actually a compressed IMF. The left-hand panel in **Figure 3** shows B_{MSH} as a function of the IMF strength. The format and color coding are the same as in the previous figures; the full colored bars are medians in IMF bins, and the dotted colored bars present medians computed for events with $B_{\text{MSH}} > B_{\text{MSP}}$. All individual points as well as all medians roughly correspond to a compression factor of about 4 that is consistent with IMF compression at the supercritical quasi-perpendicular bow shock (Spreiter and Stahara, 1980). Since the red medians in each IMF bin are the lowest, we can conclude that the compression factor decreases with the distance from the subsolar point that is consistent with early magnetosheath models (Spreiter and Stahara, 1980). Comparing the medians computed from all data (full lines) and medians corresponding to events with $B_{\text{MSH}} > B_{\text{MSP}}$ (dotted lines), we can note that both medians are about equal at the distant flank (red). It means that 1) the number of events with $B_{\text{MSH}} > B_{\text{MSP}}$ prevails and 2) the inverse gradient is not connected with an enhanced IMF compression in this region. The same is true for the near-flank (green) events with an exception of IMF below $5 nT$, and thus, we can conclude that the formation of an enlarged magnetic gradient across the flank magnetopause is not

TABLE 2 | Distributions of differences between observed R_{obs} and modeled R_{mod} magnetopause stand-off distances. Parameters of Gaussian fits (center and FWHM) are given for three magnetopause regions.

	All events		$\alpha < 30^\circ$		$30^\circ < \alpha < 60^\circ$		$\alpha > 60^\circ$	
	Center	FWHM	Center	FWHM	Center	FWHM	Center	FWHM
$B_{\text{MSH}} < B_{\text{MSP}}$	0.18	1.33	0.14	1.28	0.23	1.3	0.12	1.54
$B_{\text{MSH}} > B_{\text{MSP}}$	-0.04	1.6	-0.06	1.08	0.11	1.46	-0.16	1.75



connected with larger than usual IMF compression at the bow shock.

In order to check the conditions in the magnetosphere, we have applied the Tsyganenko (1989) model (T89 model) of the magnetic field that takes into account variations of the geomagnetic activity and computed a prediction of the magnetic field strength at the point of each magnetopause crossing. The model is parameterized with the Kp index that covers geomagnetic activity in a broad range of latitudes, and thus, it would reflect the influence of the ring current as well as auroral electrojets on the magnetospheric magnetic field. A comparison of observed and predicted magnetic fields is shown in the right-hand panel in **Figure 3**. Since the model is relatively simple and does not include the influence of upstream conditions on the magnetospheric field, the spread of points is rather large, but the medians shown by colored bars lie

approximately on the black line that signifies the identity of the predicted and measured magnetic fields. It is especially true at the small fields at flanks (green and red bars) where a great majority of events with $B_{\text{MSH}} > B_{\text{MSP}}$ (blue crosses) were observed.

3.2 Geomagnetic Activity

A combination of conclusions following from the previous figures with the fact that the magnetopause is only slightly compressed (**Figure 1**) suggests that the excess of the magnetic pressure on the magnetosheath side would be compensated by the plasma pressure on the magnetospheric side and thus a link with the geomagnetic activity. In order to check it, the $B_{\text{MSH}}/B_{\text{MSP}}$ ratio as a function of two basic geomagnetic indices, $S\text{YM-H}$ and $A\text{E}$, is shown in **Figure 4**.

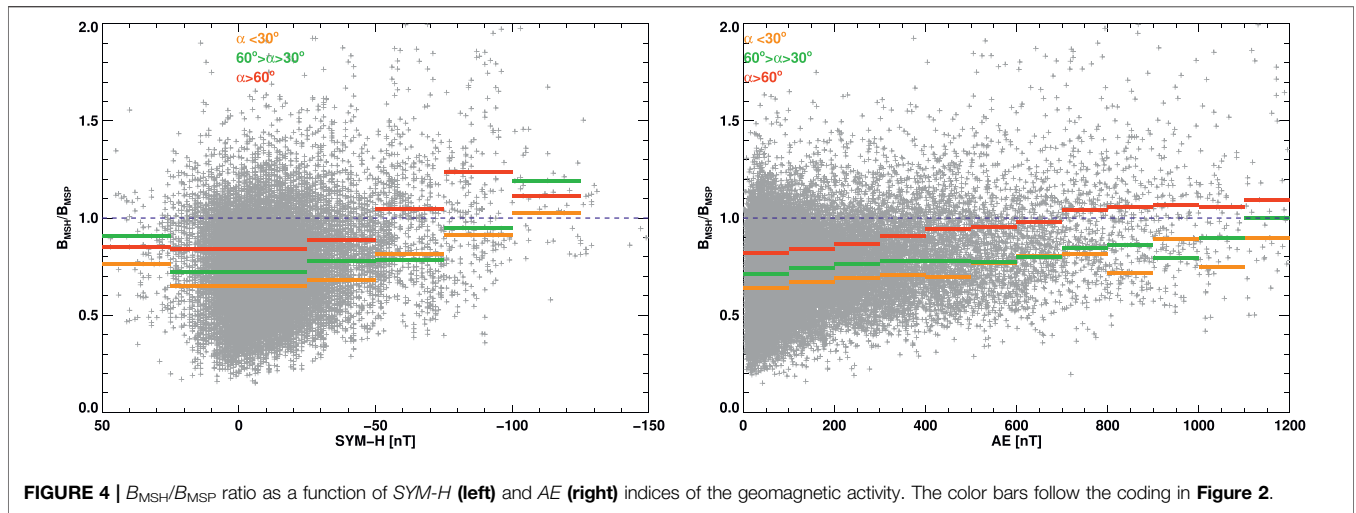


FIGURE 4 | B_{MSH}/B_{MSP} ratio as a function of *SYM-H* (left) and *AE* (right) indices of the geomagnetic activity. The color bars follow the coding in **Figure 2**.

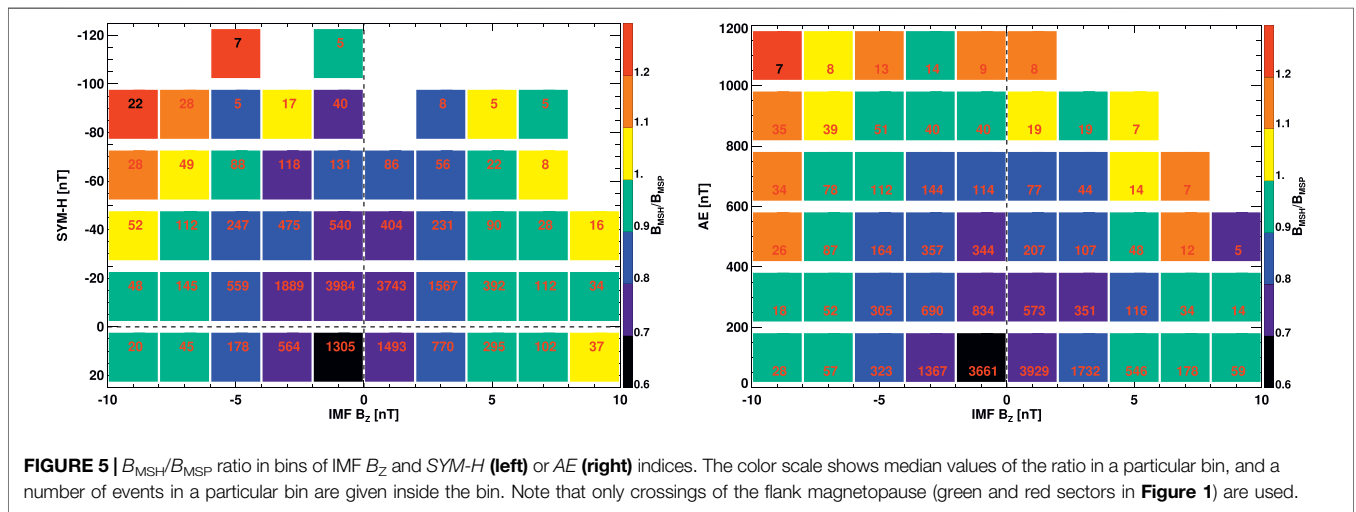


FIGURE 5 | B_{MSH}/B_{MSP} ratio in bins of IMF B_z and *SYM-H* (left) or *AE* (right) indices. The color scale shows median values of the ratio in a particular bin, and a number of events in a particular bin are given inside the bin. Note that only crossings of the flank magnetopause (green and red sectors in **Figure 1**) are used.

Since the THEMIS orbits cover predominantly the low-latitude magnetopause, *SYM-H* seems to be more appropriate, and the medians shown by color bars in the left panel reveal that the B_{MSH}/B_{MSP} ratio is about constant and does not depend on a value of the index if the magnetosphere is quiet ($SYM-H > -30 nT$), but it increases with increasing geomagnetic activity. The same conclusion follows from the right-hand panel that presents a dependence of B_{MSH}/B_{MSP} on the *AE* index. It is interesting to note that although THEMIS moves basically in the low-latitude magnetopause, the correlation of the *AE* index describing the auroral activity with the B_{MSH}/B_{MSP} ratio is slightly larger (0.17) than that with *SYM-H* index (0.12) that is predominantly affected by ring current changes, thus processes at low latitudes.

A combination of **Figures 2–4** suggests that the conditions for the creation of an inverse magnetic gradient across the flank magnetopause are large IMF dominated by perpendicular (B_Y and B_Z) components and/or enhanced geomagnetic activity. An additional analysis has shown that the correlation of the B_{MSH}/B_{MSP} ratio with IMF B_Z is 0.43 while it is only 0.30 for IMF B_Y ,

and thus, we focus on *SYM-H*, *AE*, and IMF B_Z . To find which of these factors are more important, **Figure 5** combines these parameters.

We binned data into 2 nT wide bins of IMF B_Z and then into 25 nT wide bins of *SYM-H* (left panel) and 200 nT wide bins of *AE* (right panel), respectively. For each of these bins, we counted the number of events, and if it exceeded 5, we further calculated the median of the B_{MSH}/B_{MSP} ratio. The number of events is given in each bin, and the value of the B_{MSH}/B_{MSP} median is shown by color. To be more illustrative, we use discrete colors instead of a continuous color palette. The scale is shown on the right-hand side of each panel, and numbers stand for rounded medians.

A brief look at the panels of **Figure 5** reveals that low B_{MSH}/B_{MSP} medians (blue color) require a combination of small IMF B_Z , regardless of its polarity, and a low geomagnetic activity. On the other hand, $B_{MSH}/B_{MSP} > 1.1$ (orange and red colors) can be observed nearly exceptionally during intervals of strong (< -4) negative IMF B_Z and enhanced geomagnetic activity. There are several exceptions from these rules in our statistics, but all of them

TABLE 3 | Statistics of inverse gradient observations under different solar wind driving. The first line shows a number of MP crossings under specified conditions, the second line marks a number of crossings exhibiting inverse gradient, and the third line, their ratio.

SW type	SLOW	FAST	HCS	CIR	EJECTA	MC	IS + ISA
No. of events	12,783	10,087	2,178	3,414	1857	455	412
Inv. gradient	837	655	92	733	312	183	61
Occurrence rate	0.06	0.06	0.04	0.21	0.17	0.40	0.04

are connected with a small number of events in the bins, and thus, their statistical significance is low. Although the analysis covers predominantly the magnetopause at low geomagnetic latitudes, it seems that auroral activity (*AE* index) is an important factor for the creation of an inverse magnetic gradient because it is observed always if $AE > 1000$.

3.3 Relation to Solar Wind Categories

Yermolaev et al. (2009) suggested a scheme for a classification of the solar wind into several categories. They use hourly averaged OMNI solar wind and IMF data and attribute each hour to one of nine solar wind types—slow wind (SLOW), fast wind (FAST), heliospheric current sheet (HCS), co-rotating interaction region (CIR), interplanetary coronal mass ejection that does not exhibit magnetic cloud features (EJECTA), magnetic cloud (MC), and two categories of interplanetary shocks (IS and ISA). Although the authors originally processed the 1976–2000 years, they continue with the classification till present, and a list of intervals attributed to mentioned categories are available at <ftp://ftp.iki.rssi.ru/pub/omni/catalog/>. Since the statistics presented in Figure 5 suggest a connection of an inverse magnetic gradient with geomagnetic activity, and solar wind geomagnetic effectiveness varies with the category, we have used their classification and checked a possible relation. The results are presented in Table 3. Note that we combined IS and ISA categories because the number of intervals in these categories was too low. Looking at Table 3, we can note that the occurrence rate of the inverse magnetic gradient agrees well with the results in Figure 5. It is not surprising because MCs are typical drivers of large geomagnetic storms, and they often bring a large southward IMF toward the magnetopause. On the other hand, standard upstream conditions (slow or fast solar winds) lead to the inverse gradient only exceptionally.

4 SUMMARY OF STATISTICAL RESULTS

We report a statistics of observations of the magnetic gradient across the dayside magnetopause with an emphasis on the situation when the magnetosheath magnetic field magnitude is larger than the field just inbound the magnetopause, i.e., $B_{\text{MSH}} > B_{\text{MSP}}$. Since this configuration contradicts to a general understanding of the magnetopause formation, we use the term inverse magnetic gradient for brevity. The statistics compare three regions—subsolar, near, and distant flanks. We can summarize our statistical findings as follows:

1. Median magnitudes of the $B_{\text{MSH}}/B_{\text{MSP}}$ ratio are 0.65 at the subsolar region, 0.7 at the near flank, and 0.9 at the distant

flank, respectively (Figure 1). The inverse gradient is observed more frequently across the flank magnetopause, and the occurrence rate strongly rises with the departure of the crossing local time from the noon; it is 1.5% in the subsolar region, 7% at the near flank, and 20% at the distant flank (Table 1).

2. A presence of the inverse magnetic gradient across the magnetopause is not exceptional because it is observed at about 9% of all magnetopause crossings. Moreover, the inverse magnetic gradient is a natural continuation of the trends of the $B_{\text{MSH}}/B_{\text{MSP}}$ ratio dependence on factors such as the IMF strength, cone angle (Figure 2), and geomagnetic activity (Figures 4, 5).
3. The magnetosheath magnetic field strength corresponds to its upstream source (Figure 3); the compression ratio does not depend on the $B_{\text{MSH}}/B_{\text{MSP}}$ value (not shown).
4. The magnetopause location is well predicted by the Lin et al. (2010) model; the crossings exhibiting the inverse magnetic gradient are observed slightly closer to the Earth than the model predicts (Figure 1; Table 1).
5. The $B_{\text{MSH}}/B_{\text{MSP}}$ ratio > 1 is observed for both polarities of IMF B_z , but the occurrence rate and median values of this ratio are larger for southward IMF (Figure 5).
6. The inverse gradient is observed preferentially during intervals of an enhanced geomagnetic activity described by *AE* and *SYM-H* indices (Figure 5).
7. The inverse gradient is not connected with lower than average magnetospheric magnetic field strength just inbound of the magnetopause that is well modeled by the T89 model (Figure 3).
8. Correlation coefficients between the $B_{\text{MSH}}/B_{\text{MSP}}$ ratio and B_{MSP} are 0.06 only, whereas it is 0.70 for B_{MSH} .

The preferential observations of the inverse magnetic gradient during enhanced geomagnetic activity are consistent with a classification of corresponding upstream conditions in Table 3—the largest probability of its creation occurs when the magnetosphere is affected by MCs, CMEs, or CIRs, and these structures are responsible for major geomagnetic storms (Richardson et al., 2021). The storm-time magnetosphere is characterized by an enhanced ring current that decreases the magnetic field at the Earth surface (*SYM-H* index becomes negative) and increases the magnetic field at the magnetopause. The enhancement of eastward and westward auroral electrojets during storm times leads to increase/decrease of the surface magnetic field described by *AL/AU* indices, and it again would lead to corresponding changes of the magnetic field strength at the magnetopause. Nevertheless, all these effects are implemented in the T89 model, and Figure 3

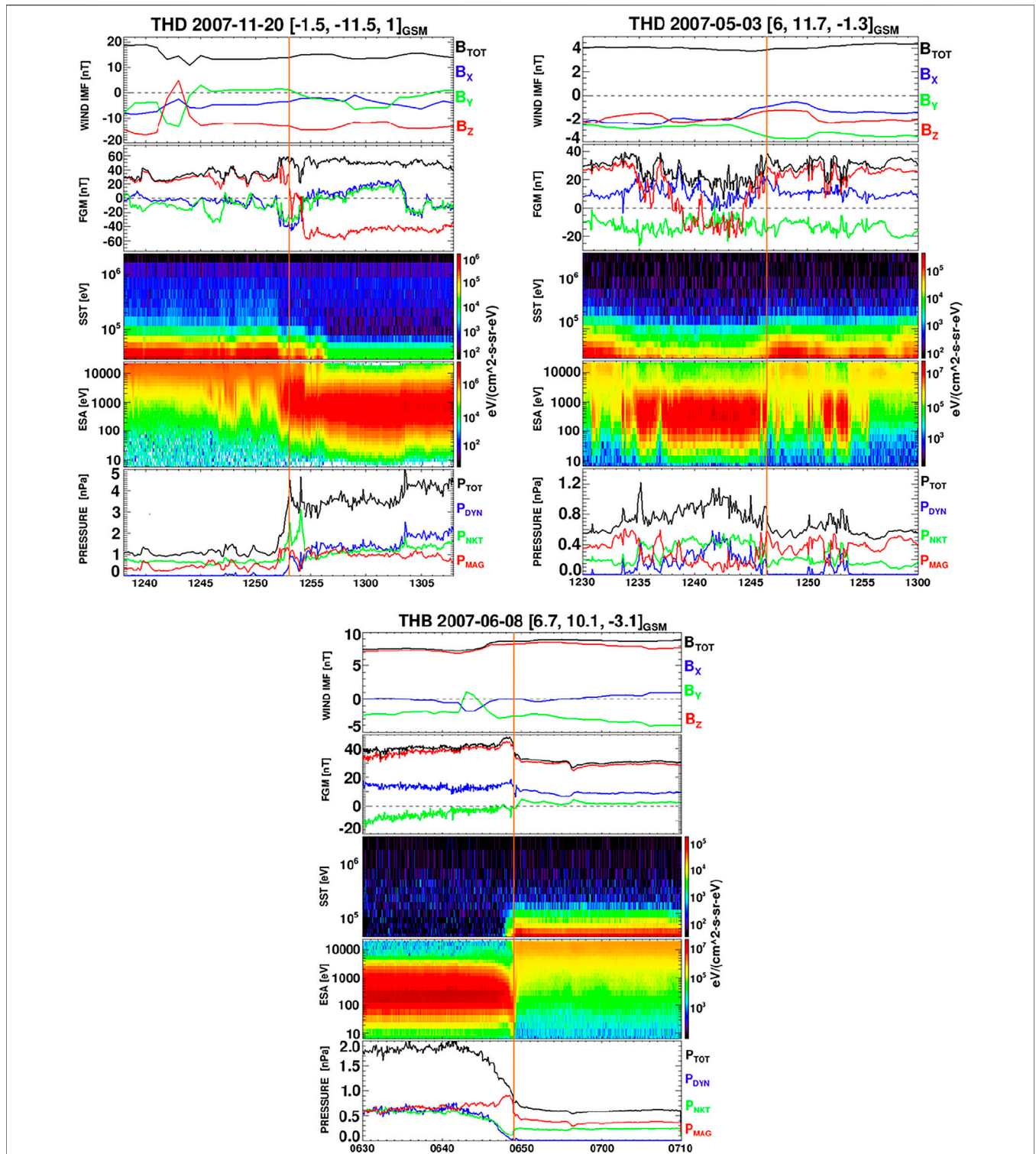


FIGURE 6 | Examples of magnetopause crossings. Left—the crossing exhibiting a strong inverse gradient under southward IMF and enhanced geomagnetic activity ($SYM-H \approx -51 \text{ nT}$, $AE \approx 212 \text{ nT}$); right—the crossing with a standard gradient under southward IMF ($SYM-H \approx -6 \text{ nT}$, $AE \approx 162 \text{ nT}$); bottom—the crossing exhibiting an inverse gradient under northward IMF ($SYM-H \approx 3 \text{ nT}$, $AE \approx 30 \text{ nT}$). The panels in each section show from top to bottom: the IMF strength and components propagated from the wind; the magnetic field measured by THEMIS; the energy flux of energetic ions from the SST instrument; and the ion energy flux from the ESA instrument; and the total pressure, P_{TOT} , (black) and its particular components: P_{DYN} (blue)—the dynamic pressure perpendicular to the model magnetopause surface, P_{NKT} (green)—a sum of ion and electron thermal pressures, and P_{MAG} (red)—the magnetic pressure. Note that P_{NKT} was computed from the ESA ground moments, and the contribution of SST represents less than 1% of the total pressure.

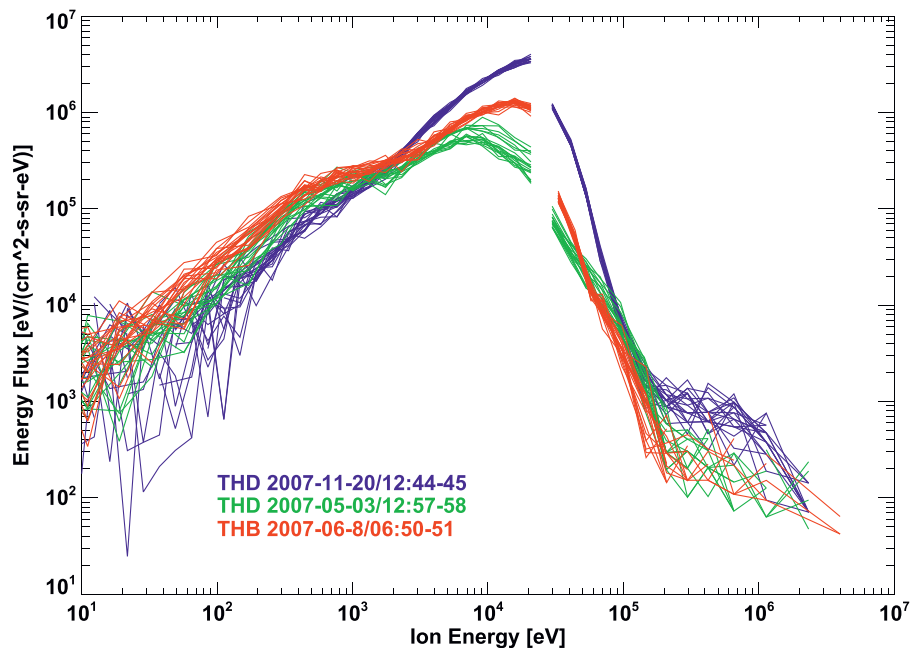


FIGURE 7 | Energetic distributions of the ion energy flux in the magnetosphere just inbound the magnetopause for events in **Figure 6**. The parts of distributions below 30 keV were determined from the ESA spectrometer and the high-energy parts from the SST detector.

shows that the distribution of the measured magnetic field around the value predicted by a model does not depend on the $B_{\text{MSH}}/B_{\text{MSP}}$ ratio. Moreover, a comparison of T89 predictions for Kp index 1 and 6 at different locations shows that the storm effect on the magnetic field at the magnetopause can be as large as +10 nT in the near flank region, but it decreases to +2 nT at the far flank, and these values cannot explain a presence of the inverse gradient because the storm currents increase B_{MSP} , but we observe $B_{\text{MSH}} > B_{\text{MSP}}$. Weigel (2010) argue that the solar wind density amplifies the geomagnetic response to the solar wind activity, but we did not find any notable effect of the upstream density on the formation of the inverse gradient; the correlation of the $B_{\text{MSH}}/B_{\text{MSP}}$ ratio with the upstream density is only 0.08.

A common understanding of the pressure balance across the magnetopause is that the sum of magnetic and plasma pressures at the magnetosheath side is balanced by a stronger magnetic field in the magnetosphere, but we are discussing events with an excess of the magnetic pressure on the magnetosheath side. The fact that the magnetopause is approximately at the position predicted by the empirical model (**Figure 1**) suggests an enhanced contribution of the magnetospheric plasma to the total pressure in a comparison with typical conditions. However, determination of plasma parameters at the magnetopause is difficult because the boundary layers on both sides of the magnetopause often contain a mix of magnetosheath and magnetospheric populations (Němeček et al., 2015), and even low-energy plasma from a plasmasphere (McFadden et al., 2008b) can be observed at the magnetopause during storm-time intervals. For this reason, we will demonstrate the conditions leading to the creation of the inverse gradient for several cases.

5 SUPPORTING CASE STUDY

In accord with the above statistical study, we have chosen three events. First of them occurred during the geomagnetic storm under a strong southward IMF and represents a typical example of the inverse gradient, $B_{\text{MSH}} \approx 2.2 B_{\text{MSP}}$. This event is contrasted with another crossing observed under similar conditions but with a standard gradient, $B_{\text{MSH}} < B_{\text{MSP}}$. The third example is a representative of a group of crossings exhibiting the inverse gradient under a northward IMF. The basic data for these three crossings are shown in three sections of **Figure 6**.

Comparison of the figure sections reveals that both magnetopause crossings observed under southward IMF exhibit relatively thick boundary layer characterized by staircase like (left-hand section) or smooth (right-hand section) transition of the B_z component from the negative value in the magnetosheath to the positive value on the magnetospheric side and mixed plasma populations on both sides of the magnetopause. On the other hand, the northward IMF (bottom section) leads to a sharp MP crossing with abrupt changes of the ion density and temperature, as it can be seen in the bottom section of the figure. These features distinguish the flank and subsolar magnetopause because Němeček et al. (2015) presented statistically that a thick boundary layer is a consequence of cusp reconnection, and thus, it is formed by northward IMF.

The formation of the boundary layer at the low-latitude flanks for strong southward IMF is affected by the presence of dayside extension of the plasma sheet that is supplied by intensive reconnection. This reconnection increases cross-tail potential driving magnetospheric current systems that modify the

magnetic field at the magnetopause. Enhanced current heats the magnetospheric plasma and brings new charge carriers to the boundary layer. As a result, the magnetospheric plasma pressure is enhanced, balances the magnetosheath magnetic pressure, and keeps the magnetopause in an equilibrium state in the southward events with inverse magnetic gradient. We plot the energy distributions of magnetospheric ions just inbound of the magnetopause in **Figure 7** for events shown in **Figure 6**. The figure shows a merged ion energy flux distribution from ESA and SST analyzers. Although there is an energy gap between the two analyzers, one can see that the maximum of the ion energy flux is above the range of the ESA analyzer (≈ 30 keV) for the blue distribution that belongs to the event exhibiting a strong inverse gradient (**Figure 6**, left-hand section).

Consequently, we can suppose that the temperature of the ion population is larger than that calculated as the moment of the ESA distribution, and it causes an apparent lack of the magnetospheric pressure demonstrated in the bottom panels in all sections of **Figure 6**. When the southward IMF is not so strong (right-hand section) of **Figure 6**, the magnetospheric currents are weaker, and density and temperature in the magnetosphere are lower (green distribution in **Figure 7**), and we observe a standard magnetic gradient across the magnetopause. This explanation expects a large cross-tail potential for events with the inverse magnetic gradient, and it is consistent with the PCN index being 7 mV/m for the example in the left section of **Figure 6**, whereas it is only 1.5 mV/m for the event with the standard magnetic gradient shown in the middle section.

The northward crossing (bottom section of **Figure 6**) exhibits a clear plasma depletion layer at the magnetosheath side (Zwan and Wolf, 1976) characterized by an enhancement of the magnetic field complemented with a density depletion in front of the magnetopause. Nevertheless, the magnetosheath magnetic field outside this layer is still larger than that in the magnetosphere in spite of the fact that the geomagnetic activity is low, and it was low within preceding 12 h. The pressure balance calculated using the plasma moments from the ion spectrometer shows a lack of the pressure in the magnetosphere (last panel), but, similarly to the southward event, the ion density and temperature are underestimated because the maximum of the ion distribution is at the upper edge of the spectrometer energy range (red curve in **Figure 7**). However, mechanisms leading to such hot and dense plasma in the magnetosphere layer adjacent to the magnetopause should be further investigated.

REFERENCES

- Angelopoulos, V. (2008). The THEMIS mission. *Space Sci. Rev.* 141, 5–34. doi:10.1007/s11214-008-9336-1
- Artemyev, A. V., Angelopoulos, V., Runov, A., Wang, C.-P., and Zelenyi, L. M. (2017). Properties of the Quatorial Magnetotail Flanks ~ 50 – $200 R_E$ downtail. *J. Geophys. Res. Space Phys.* 122, 11917–11930. doi:10.1002/2017JA024723

6 CONCLUSION

We present a statistical study of the magnetic field gradient across the magnetopause with an emphasis on the flank magnetopause and events when the magnetospheric magnetic field was lower than that in the adjacent magnetosheath. Based on the above discussion, we can believe that we understand the formation of magnetopause layers that can lead to an inverse magnetic gradient across the magnetopause for southward IMF. The intensive reconnection caused by a large southward IMF increases cross-tail potential driving strong magnetospheric currents that overheat the magnetospheric plasma and bring it to the magnetopause. The presence of such plasma leads to a diamagnetic effect (decrease of the magnetospheric magnetic field) and increases the plasma pressure on the magnetospheric side. We have shown that the intensity of these processes increases with the IMF strength, and thus, we can conclude that IMF strength influences the processes in the magnetosphere much more than we expected so far.

DATA AVAILABILITY STATEMENT

Publicly available datasets were analyzed in this study. This data can be found here: <http://cdaweb.gsfc.nasa.gov/>

AUTHOR CONTRIBUTIONS

The article is a result of efforts of all authors, and their particular contributions are as follows: Data processing—THEMIS, KG and JS; methodology, ZN; data analysis and interpretation, ZN and JS; software and visualization, KG and JS; original draft preparation, ZN; contribution to data interpretation and enhanced discussion, GP.

FUNDING

The work was supported by the Czech Science Foundation under Contract 21-26463S.

ACKNOWLEDGMENTS

The authors thank the Wind and THEMIS teams for the magnetic field and plasma data available *via* <http://cdaweb.gsfc.nasa.gov/>. They also thank professor Vitek for his continuous support.

- Auster, H. U., Glassmeier, K. H., Magnes, W., Aydogar, O., Baumjohann, W., Constantinescu, D., et al. (2008). The THEMIS Fluxgate Magnetometer. *Space Sci. Rev.* 141, 235–264. doi:10.1007/s11214-008-9365-9
- Berchem, J., and Russell, C. T. (1982). The Thickness of the Magnetopause Current Layer: ISEE 1 and 2 Observations. *J. Geophys. Res.* 87, 2108–2114. doi:10.1029/ja087ia04p02108
- Borovsky, J. E., Elphic, R. C., Funsten, H. O., and Thomsen, M. F. (1997). The Earth's Plasma Sheet as a Laboratory for Flow Turbulence in High- β MHD. *J. Plasma Phys.* 57, 1–34. doi:10.1017/s0022377896005259

- Cai, D., Storey, L. R. O., and Neubert, T. (1990). Kinetic Equilibria of Plasma Shear Layers. *Phys. Fluids B: Plasma Phys.* 2, 75–85. doi:10.1063/1.859541
- Coroniti, F. V., and Kennel, C. F. (1972). Changes in Magnetospheric Configuration during the Substorm Growth Phase. *J. Geophys. Res.* 77, 3361–3370. doi:10.1029/ja077i019p03361
- Fadanelli, S., Faganello, M., Califano, F., Cerri, S. S., Pegoraro, F., and Lavraud, B. (2018). North-South Asymmetric Kelvin-Helmholtz Instability and Induced Reconnection at the Earth's Magnetospheric Flanks. *J. Geophys. Res. Space Phys.* 123, 9340–9356. doi:10.1029/2018JA025626
- Fu, H. S., Khotyaintsev, Y. V., Vaivads, A., André, M., and Huang, S. Y. (2012). Occurrence Rate of Earthward-Propagating Dipolarization Fronts. *Geophys. Res. Lett.* 39, L10101. doi:10.1029/2012gl051784
- Fujimoto, M., Terasawa, T., Mukai, T., Saito, Y., Yamamoto, T., and Kokubun, S. (1998). Plasma Entry from the Flanks of the Near-Earth Magnetotail: Geotail Observations. *J. Geophys. Res.* 103, 4391–4408. doi:10.1029/97JA03340
- Haaland, S., Paschmann, G., Øieroset, M., Phan, T., Hasegawa, H., Fuselier, S. A., et al. (2020). Characteristics of the Flank Magnetopause: MMS Results. *J. Geophys. Res. Space Phys.* 125, e2019JA027623. doi:10.1029/2019JA027623
- Haaland, S., Runov, A., Artemyev, A., and Angelopoulos, V. (2019). Characteristics of the Flank Magnetopause: THEMIS Observations. *J. Geophys. Res. Space Phys.* 124, 3421–3435. doi:10.1029/2019JA026459
- Hasegawa, H., Fujimoto, M., Phan, T.-D., Rème, H., Balogh, A., Dunlop, M. W., et al. (2004). Transport of Solar Wind into Earth's Magnetosphere through Rolled-Up Kelvin-Helmholtz Vortices. *Nature* 430 (7001), 755–758. doi:10.1038/nature02799
- Hasegawa, H., Retinò, A., Vaivads, A., Khotyaintsev, Y., André, M., Nakamura, T. K. M., et al. (2009). Kelvin-Helmholtz Waves at the Earth's Magnetopause: Multiscale Development and Associated Reconnection. *J. Geophys. Res.* 114, 12207. doi:10.1029/2009JA014042
- Hasegawa, H. (2012). Structure and Dynamics of the Magnetopause and its Boundary Layers. *Monogr. Environ. Earth Planets* 1 (2), 71–119. doi:10.5047/meep.2012.00102.0071
- Jelínek, K., Němeček, Z., and Šafránková, J. (2012). A New Approach to Magnetopause and bow Shock Modeling Based on Automated Region Identification. *J. Geophys. Res.* 117, A05208. doi:10.1029/2011JA017252
- Kavosi, S., and Raeder, J. (2015). Ubiquity of Kelvin-Helmholtz Waves at Earth's Magnetopause. *Nat. Commun.* 6, 7019. doi:10.1038/ncomms8019
- Kistler, L. M. (2020). Ionospheric and Solar Wind Contributions to the Storm-Time Near-Earth Plasma Sheet. *Geophys. Res. Lett.* 47, e2020GL090235. doi:10.1029/2020GL090235
- Kistler, L. M., Mouikis, C. G., Asamura, K., Yokota, S., Kasahara, S., Miyoshi, Y., et al. (2019). Cusp and Nightside Auroral Sources of O⁺ in the Plasma Sheet. *J. Geophys. Res. Space Phys.* 124, 10036–10047. doi:10.1029/2019JA027061
- Lavraud, B., and Jordanova, V. K. (2007). Modeling the Effects of Cold-Dense and Hot-Tenuous Plasma Sheet on Proton Ring Current Energy and Peak Location. *Geophys. Res. Lett.* 34, L02102. doi:10.1029/2006GL027566
- Lavraud, B., Thomsen, M. F., Wing, S., Fujimoto, M., Denton, M. H., Borovsky, J. E., et al. (2006). Observation of Two Distinct Cold, Dense Ion Populations at Geosynchronous Orbit: Local Time Asymmetry, Solar Wind Dependence and Origin. *Ann. Geophys.* 24, 3451–3465. doi:10.5194/angeo-24-3451-2006
- Lemaire, J., Rycroft, M. J., and Roth, M. (1979). Control of Impulsive Penetration of Solar Wind Irregularities into the Magnetosphere by the Interplanetary Magnetic Field Direction. *Planet. Space Sci.* 27, 47–57. doi:10.1016/0032-0633(79)90146-6
- Li, K., Haaland, S., Eriksson, A., André, M., Engwall, E., Wei, Y., et al. (2013). Transport of Cold Ions from the Polar Ionosphere to the Plasma Sheet. *J. Geophys. Res. Space Phys.* 118, 5467–5477. doi:10.1002/jgra.50518
- Lin, R. L., Zhang, X. X., Liu, S. Q., Wang, Y. L., and Gong, J. C. (2010). A Three-Dimensional Asymmetric Magnetopause Model. *J. Geophys. Res.* 115, A04207. doi:10.1029/2009JA014235
- Lukin, A. S., Panov, E. V., Artemyev, A. V., Petrukovich, A. A., Haaland, S., Nakamura, R., et al. (2020). Comparison of the Flank Magnetopause at Near-Earth and Lunar Distances: MMS and ARTEMIS Observations. *J. Geophys. Res. Space Phys.* 125, e2020JA028406. doi:10.1029/2020JA028406
- McFadden, J. P., Carlson, C. W., Larson, D., Bonnell, J., Mozer, F. S., Angelopoulos, V., et al. (2008b). Structure of Plasmaspheric Plumes and Their Participation in Magnetopause Reconnection: First Results from THEMIS. *Geophys. Res. Lett.* 35, L17S10. doi:10.1029/2008gl033677
- McFadden, J. P., Carlson, C. W., Larson, D., Ludlam, M., Abiad, R., Elliott, B., et al. (2008a). The THEMIS ESA Plasma Instrument and In-Flight Calibration. *Space Sci. Rev.* 141, 277–302. doi:10.1007/s11214-008-9440-2
- McPherron, R. L., Hsu, T.-S., Kissinger, J., Chu, X., and Angelopoulos, V. (2011). Characteristics of Plasma Flows at the Inner Edge of the Plasma Sheet. *J. Geophys. Res.* 116, A00133. doi:10.1029/2010JA015923
- Mouikis, C. G., Bingham, S. T., Kistler, L. M., Farrugia, C. J., Spence, H. E., Reeves, G. D., et al. (2019). The Storm-Time Ring Current Response to ICMs and CIRs Using Van Allen Probe Observations. *J. Geophys. Res. Space Phys.* 124, 9017–9039. doi:10.1029/2019JA026695
- Mouikis, C. G., Kistler, L. M., Liu, Y. H., Klecker, B., Korth, A., and Dandouras, I. (2010). H⁺ and O⁺ content of the Plasma Sheet at 15–19 Re as a Function of Geomagnetic and Solar Activity. *J. Geophys. Res.* 115, A00J16. doi:10.1029/2010JA015978
- Nakamura, T. K. M., Hasegawa, H., and Shinohara, I. (2010). Kinetic Effects on the Kelvin-Helmholtz Instability in Ion-To-Magnetohydrodynamic Scale Transverse Velocity Shear Layers: Particle Simulations. *Phys. Plasmas* 17, 042119. doi:10.1063/1.3385445
- Němeček, Z., Šafránková, J., Kruparova, O., Přeč, L., Jelínek, K., Dušík, Š., et al. (2015). Analysis of Temperature versus Density Plots and Their Relation to the LBL Formation under Southward and Northward IMF Orientations. *J. Geophys. Res. Space Phys.* 120, 3475–3488. doi:10.1002/2014JA020308
- Němeček, Z., Šafránková, J., Lopez, R. E., Dušík, Š., Nouzák, L., Přeč, L., et al. (2016). Solar Cycle Variations of Magnetopause Locations. *Adv. Space Res.* 58, 240–248. doi:10.1016/j.asr.2015.10.012
- Němeček, Z., Šafránková, J., and Šimůnek, J. (2020). An Examination of the Magnetopause Position and Shape Based upon New Observations. *Geophys. Monogr. Ser.* 248, 135–151. doi:10.1002/9781119509592.ch8
- Němeček, Z., Šafránková, J., Zastenker, G. N., Pišoft, P., and Jelínek, K. (2002). Low-frequency Variations of the Ion Flux in the Magnetosheath. *Planet. Space Sci.* 50, 567–575. doi:10.1016/S0032-0633(02)00036-3
- Paschmann, G., Sonnerup, B. U. Ö., Papamastorakis, I., Sckopke, N., Haerendel, G., Bame, S. J., et al. (1979). Plasma Acceleration at the Earth's Magnetopause: Evidence for Reconnection. *Nature* 282, 243–246. doi:10.1038/282243a0
- Richardson, I. G., Cliver, E. W., and Cane, H. V. (2021). Sources of Geomagnetic Storms for Solar Minimum and Maximum Conditions during 1972–2000. *Geophys. Res. Lett.* 48, 2569–2572.
- Šafránková, J., Přeč, L., Němeček, Z., and Sauvaud, J. A. (2002). Density Profile in the Magnetosheath Adjacent to the Magnetopause. *Adv. Space Res.* 30, 1693–1703. doi:10.1016/S0273-1177(02)00438-6
- Samsonov, A. A., Němeček, Z., Šafránková, J., and Jelínek, K. (2012). Why Does the Subsolar Magnetopause Move Sunward for Radial Interplanetary Magnetic Field? *J. Geophys. Res.* 117, A05221. doi:10.1029/2011JA017429
- Sandholt, P. E., Farrugia, C. J., Cowley, S. W. H., Denig, W. F., Lester, M., Moen, J., et al. (1999). Capture of Magnetosheath Plasma by the Magnetosphere during Northward IMF. *Geophys. Res. Lett.* 26, 2833–2836. doi:10.1029/1999gl900600
- Shevryev, N. N., Zastenker, G. N., Nozdachev, M. N., Němeček, Z., Šafránková, J., and Richardson, J. D. (2003). High and Low Frequency Large Amplitude Variations of Plasma and Magnetic Field in the Magnetosheath: Radial Profile and Some Features. *Adv. Space Res.* 31, 1389–1394. doi:10.1016/S0273-1177(03)00008-5
- Song, P., and Russell, C. T. (1992). Model of the Formation of the Low-Latitude Boundary Layer for Strongly Northward Interplanetary Magnetic Field. *J. Geophys. Res.* 97, 1411. doi:10.1029/91ja02377
- Sonnerup, B. U. Ö., Paschmann, G., Papamastorakis, I., Sckopke, N., Haerendel, G., Bame, S. J., et al. (1981). Evidence for Magnetic Field Reconnection at the Earth's Magnetopause. *J. Geophys. Res.* 86, 10049. doi:10.1029/ja086ia12p10049
- Sorathia, K. A., Merkin, V. G., Ukhorskiy, A. Y., Allen, R. C., Nykyri, K., and Wing, S. (2019). Solar Wind Ion Entry into the Magnetosphere during Northward IMF. *J. Geophys. Res. Space Phys.* 124, 5461–5481. doi:10.1029/2019JA026728
- Spreiter, J. R., and Stahara, S. S. (1980). A New Predictive Model for Determining Solar Wind-Terrestrial Planet Interactions. *J. Geophys. Res.* 85, 6769. doi:10.1029/ja085ia12p06769
- Spreiter, J. R., Summers, A. L., and Alksne, A. Y. (1966). Hydromagnetic Flow Around the Magnetosphere. *Planet. Space Sci.* 14, 223–253. doi:10.1016/0032-0633(66)90124-3

- Thomsen, M. F., Borovsky, J. E., Skoug, R. M., and Smith, C. W. (2003). Delivery of Cold, Dense Plasma Sheet Material into the Near-Earth Region. *J. Geophys. Res.* 108, 1151. doi:10.1029/2002JA009544
- Toledo-Redondo, S., André, M., Khotyaintsev, Y. V., Vaivads, A., Walsh, A., Li, W., et al. (2016). Cold Ion Demagnetization Near the X-Line of Magnetic Reconnection. *Geophys. Res. Lett.* 43, 6759–6767. doi:10.1002/2016gl069877
- Treumann, R. A., Labelle, J., and Bauer, T. M. (1995). “Diffusion Processes: An Observational Perspective,” in *Geophysical Monograph Series*. Editor D. Chiang (Washington DC: American Geophysical Union), 90, 331.
- Tsyganenko, N. A. (1989). A Magnetospheric Magnetic Field Model with a Warped Tail Current Sheet. *Planet. Space Sci.* 37, 5–20. doi:10.1016/0032-0633(89)90066-4
- Tsyganenko, N. A., and Andreeva, V. A. (2015). A Forecasting Model of the Magnetosphere Driven by an Optimal Solar Wind Coupling Function. *J. Geophys. Res. Space Phys.* 120, 8401–8425. doi:10.1002/2015ja021641
- Weigel, R. S. (2010). Solar Wind Density Influence on Geomagnetic Storm Intensity. *J. Geophys. Res.* 115, A09201. doi:10.1029/2009JA015062
- Wing, S., Johnson, J. R., Chaston, C. C., Echim, M., Escoubet, C. P., Lavraud, B., et al. (2014). Review of Solar Wind Entry into and Transport within the Plasma Sheet. *Space Sci. Rev.* 184, 33–86. doi:10.1007/s11214-014-0108-9
- Yermolaev, Y. I., Nikolaeva, N. S., Lodkina, I. G., and Yermolaev, M. Y. (2009). Catalog of Large-Scale Solar Wind Phenomena during 1976–2000. *Cosmic Res.* 47, 81–94. doi:10.1134/S0010952509020014
- Yu, Y., Chen, Z., and Chen, F. (2020). Cold and Dense Plasma Sheet Caused by Solar Wind Entry: Direct Evidence. *Atmosphere* 11, 831. doi:10.3390/atmos11080831
- Zastenker, G. N., Nozdachev, M. N., Němeček, Z., Šafránková, J., Paularena, K. I., Richardson, J. D., et al. (2002). Multispacecraft Measurements of Plasma and Magnetic Field Variations in the Magnetosheath: Comparison with Spreiter Models and Motion of the Structures. *Planet. Space Sci.* 50, 601–612. doi:10.1016/S0032-0633(02)00039-9
- Zwan, B. J., and Wolf, R. A. (1976). Depletion of Solar Wind Plasma Near a Planetary Boundary. *J. Geophys. Res.* 81, 1636–1648. doi:10.1029/ja081i010p01636

Conflict of Interest: The authors declare that the research was conducted in the absence of any commercial or financial relationships that could be construed as a potential conflict of interest.

Publisher’s Note: All claims expressed in this article are solely those of the authors and do not necessarily represent those of their affiliated organizations, or those of the publisher, the editors, and the reviewers. Any product that may be evaluated in this article, or claim that may be made by its manufacturer, is not guaranteed or endorsed by the publisher.

Copyright © 2021 Němeček, Grygorov, Šafránková, Šimůnek and Pi. This is an open-access article distributed under the terms of the Creative Commons Attribution License (CC BY). The use, distribution or reproduction in other forums is permitted, provided the original author(s) and the copyright owner(s) are credited and that the original publication in this journal is cited, in accordance with accepted academic practice. No use, distribution or reproduction is permitted which does not comply with these terms.